GSA Data Repository 2016345

Volatile dilution during magma injections and implications for volcano explosivity

Cassidy et al.

APPENDIX

Supplementary methods

Raman Spectroscopy

All Raman spectroscopy analyses were conducted on a Jobin Yvon Horiba instrument connected to an Olympus BX41 machine. A 488 nm Ar+ laser was used to excite the sample with a 50x objective, an exposure time of 25 seconds, and 40 repetition cycles to improve the signal to noise ratio. The Raman was set with a laser attenuation of 25% with respect to the total laser power, this was measured at the sample to be 1 mW, a 300 1/mm grating, confocal hole of 400 μm, and slit of 100 μm. Backscattered Raman radiation was collected over a range from 50 to 4000 cm^{-1}, and elastically scattered photons were suppressed via a sharp edge filter. The instrument was calibrated using a silicon standard. The Labspec program was used to collect the spectra and an internal intensity correction (ICS HORIBA) was used to correct the detector intensities. Prior to processing, a wave number dependent intensity correction from Long (1977) has been applied to all the spectra. Scaled optical light images were taken using an in-built microscope camera to map the melt inclusions in the crystal and to measure exposed melt inclusion areas using Image J. When targeting melt inclusions, spectra with crystal interactions were discarded, so that only melt inclusions with no or minimal (<10%) crystallization (either post-entrapment, or contribution from the host) were measured, as qualitatively assessed using backscattered SEM imagery. A less intense beam (0.01%), was focused at the surface and then trial analyses were conducted on the melt inclusions for a few minutes to check if spectra contained a signature of the host crystal. 75% were discarded due to host crystal contamination. A few larger melt inclusions were independently measured with FTIR, producing H_2O contents that overlap with those measured with the Raman. Five dacitic glasses with known H_2O contents (using Fourier Transforming Infra-Red (FTIR), were measured on the Raman five times and averaged to calibrate the intensities gained from the Raman analysis (Table DR1). The resulting calibration had an R^2 of 0.99 (Fig. DR1). The standard error of the mean was calculated using the standard deviation of multiple measurements of Raman intensities on the same known dacitic glasses (Table DR1). This produced an average error of 0.17% and a maximum of 0.22%. The data table for the Raman H_2O contents, along with crystal size, melt inclusion size, distance from the rim, and melt inclusion compositions can be found in Table DR4.

EPMA, SEM and FTIR procedures

After Raman analysis, the polished sections were carbon coated for electron probe microanalysis (EPMA) and scanning electron microscope (SEM) analysis. Plagioclase compositional traverses and melt inclusion glasses were measured with electron microprobe at the University of Mainz, using diffuse beam (5 microns) and correcting for

Na drift. All analyses used an accelerating voltage of 15 kV. For plagioclase a spot size of 4 μm and a 100 nA beam current was used. For glasses, a 10 μm spot was used with a beam current of 60 nA for Cl, F, S, P, Cr and Ni, and 4 nA for all other elements, with counting times of 50–200s per analysis. During glass measurements, Na peaks were counted first to avoid significant migration during the run. Only some melt inclusions measured with the Raman were sufficiently large enough also to measure with EPMA. Doubly polished wafers of 70 μm thickness of feldspar crystals with melt inclusions were prepared for FTIR analysis at the University of Mainz. H_2O concentrations were calculated using absorption coefficients of 68 L mol^{-1} at 3650 nm from Yamashita et al., 1997. Glass densities were calculated from the relation after Olhorst et al, 2001 using dry densities calculated from partial-molar volumes of the major oxides (Lange and Carmichael 1990). These densities were then corrected for typical H_2O contents using equation 2 in Olhost et al. (2001) for dacite compositions.

Post Entrapment Crystallization

This study focused on concentric zoned plagioclase, other crystals that display more complex textures (such as spongy, boxy-cellular) were avoided, as it is unclear if these crystals grew from progressively from core to rim (e.g. skeletal growth) and thus may affect the timing of entrapment of such melt inclusions. Post entrapment crystallization (PEC) of the melt inclusions was minimal, however to test what effect PEC could have on predicted temperatures, all melt inclusions were corrected for 20% crystallization of more albitic plagioclase using the approach of Humphreys et al. (2010). Despite this relatively large amount of PEC, this had only minimal effects on estimated temperatures (<15 °C), similar to the error associated with the plagioclase thermometer (Waters and Lange, 2015). PEC is generally thought to have a minimal effect on H_2O concentrations (Steele-Macinnis et al., 2011).

Magma Temperature Estimation

Plagioclase composition is both a function of temperature and H_2O, this means it is hard to provide a test of equilibrium for this geothermometer because typically we do not know one or both of those values. An approximate test can be made by comparing the range of plagioclase compositions grown in in melt with those data used to calibrate the hygrometer in Lange, 2009 and Figure 3 in Waters and Lange 2015. Liquid anorthite values were calculated (Equation 7a and B in Waters and Lange, 2015) and plotted versus anorthite in plagioclase as in figure 3A in Waters and Lange 2015 (Fig. DR8). Those values which deviated from the experimental constraints used to test the model were discarded as being xeno/antecrystic or out of equilibrium (Fig. DR8).

In the case that these magmas were H_2O under saturated, the Waters and Lange (2015) model is still able to accurately calculate magma temperatures, as the composition of plagioclase in a given liquid is a function of temperature and wt% H_2O in the melt, regardless of varying H_2O saturation conditions. As a comparison to the Waters and Lange, 2015 model, we also used the hygrometer model of Putirka et al. (2005). This produces the same pattern in temperature fluctuations as seen in Figure 1, however often offset to lower temperatures (~40 °C). The plot for the temperatures calculated against anorthite can be found in Fig. DR9.

Jeffery et al., 2013 also estimate temperatures for the 2007 magma based on plagioclase-melt thermometry, using the Putirka et al., 2005 model. These range from

1151 - 1164 °C (average = 1160 °C; n = 303), and are therefore significantly higher than our estimations for the 2014 magma (985 – 1110°C; average 1062°C, Table DR4). Estimated H_2O contents for the 2007 magma from Jeffrey et al., (2013) range from 0.12 – 2.29 wt%, 1σ=0.57 wt% using the difference method and 1.5-1.9 wt% using plagioclase-melt hygrometry, thus occupying a similar range to our FTIR and Raman measurements on the 2014 melt inclusions (0.45 - 2.3 wt%).

Magma reservoir pressure estimation

The value of 100 MPa was employed as a magma storage pressure in some of the calculations made (e.g. Waters and Lange thermometer and volatile solubility from Zhang et al., 2007, see below). The value was estimated using the calculations of Papale et al., 2006 for volatile saturation pressures for the melt inclusions with the highest CO_2 and H_2O contents from FTIR data (Table DR5), which gave values of 80–90 MPa. This result can be considered a minimum estimate given that the system was likely under-saturated. An upper constraint can be gained by examining phase relations from experimental studies on systems that have similar compositions (e.g. Rader and Larsen, 2013). At 1000 °C, amphibole forms under pressures >120 MPa. Moreover, therefore the lack of abundant amphibole found in the Kelud 2014 pumice suggests that the magmas were stored at lower pressures than 120 MPa. The estimate of 100 MPa equates to a magma storage depth of ~4 km (using an approximate lithostatic pressure gradient of 25 MPa km^{-1}). This depth concurs with clusters of earthquakes located at 3–4 km under Kelud in the weeks leading up to the 2014 eruption (Global Volcanism Program report). We therefore consider 100 MPa a first order estimate for the Kelud magmatic system until better constraints become available.

Diffusion of H_2O

H_2O diffusion is driven by gradients in H_2O activity rather than in H_2O concentration (Qin et al., 1992). This is because the difference between the pressure within an inclusion and external pressure is estimated to be small (Burnham, 1979). To this end, activities for melt inclusion and carrier liquid compositions (assumed to be the matrix glass composition) were calculated to estimate the potential H_2O activity gradient. The activity gradient between the melt inclusions and carrier melt was calculated at -0.07, which is comparable with the low values of ~0.04 that Hartley et al. (2015) argued may have been too small to promote H^+ diffusion through olivine host crystals (Hartley et al. 2015). Indeed, Gaetani et al., (2012) stated that "low-H_2O melt inclusions have the capacity to preserve a reliable record of H_2O and CO_2 in the melt at the time of entrapment" as they are not significantly affected by diffusive reequilibration.

In the case that a H_2O activity gradient of -0.07 was sufficient to drive reequilibration between the H_2O in the carrier melt and trapped in melt inclusions, approximate timescales for this process have been estimated assuming that diffusion can occur at very low activity gradients. A melt inclusion reequilibration model based on the model of Bucholz et al. (2013), which calculates the analytical solution for symmetrical H^+ diffusion through a spherical host crystal with a spherical inclusion at its center (Qin et al., 1992).. A range of different conditions were used based on the crystal host size, melt inclusion diameter and temperature. Initial and final H_2O contents were taken from the analyses made in this study (Table DR4). This was done so that we could explore the full range of timescales estimated for the exact conditions appropriate for this study.

Diffusion timescales were calculated using hydrogen diffusivities calculated from Johnson et al. (2013) and two different partition coefficients for hydrogen in plagioclase: 0.004 from Johnson, (2005) and 0.01 from Hamada et al. (2011). This provided a large range of diffusion timescales from a week to several months (Table DR3) for the reequilibration of H_2O with the carrier liquid. This may explain why H_2O contents in the melt inclusions were preserved whilst in storage. As the H_2O content of the carrier melt fluctuated between relatively H_2O -rich and H_2O -poor states, the melt inclusions may not have had enough time to reequilibrate with the external conditions before they changed again. As H_2O contents are unaffected by MI size, crystal size and distance from rim (i.e. diffusion effects; fig. DR3), these calculations may thus go some way to explaining why these H_2O contents may be preserved, suggesting that either diffusion was too slow in this instance (weeks to months) or the activity gradient was too small to allow diffusion to take place in the first place.

Temperature driven solubility changes affecting H_2O contents

Heating also reduces the solubility of dissolved H_2O in the melt, which could lead to H_2O exsolution (Ruprecht and Bachman, 2010). However, solubility calculations made from equations in Zhang et al., (2007) for rhyolites, show that even the largest temperature fluctuation observed (80 °C) at 100 MPa (estimated from volatile saturation pressures, see appendix) causes only a minor reduction in H_2O solubility (0.15%). For this reason magma H_2O content reduction via dilution with a H_2O -poor magma recharge is more likely.

Crystallinity calculations

Phenocryst content and crystal aspect ratio was calculated using 20 photomicrographs of thin sections for both the 2007 dome rock and the 2014 pumice. The images were scaled and thresholded in ImageJ, and measurements of crystal aspect ratio and phenocryst content were averaged from >1000 crystals. This was corrected for porosity (calculated with image analysis of multiple BSE images, 45% in 2014 pumice and 10% in 2007 dome rock) to achieve a pore-free phenocryst content, to attempt to emulate the crystallinity in the magma reservoir, before microlite crystallization upon ascent. The phenocryst content of 2014 pumice ranges from 53-75% (mean: 59%) and crystal aspect ratio of 1.88, whereas the crystallinity for the 2007 dome products ranges from 43-63% (mean, 53%) and a crystal aspect ratio of 1.86. However the 2007 crystallinity in particular must be considered as maximum considering the potential for further phenocryst growth upon slow ascent and cooling during dome emplacement near the surface, which would not have affected the 2014 magma phenocryst content to the same extent. The lower crystallinity of the 2007 magma is likely a consequence of the higher temperatures estimated for the 2007 magma in comparison to the 2014 magma. This also means that bulk viscosity of the 2007 magmas was likely significantly lower than that of the 2014 magma. These crystallinity measurements for the 2014 erupted pumice were used in Fig. 3 to estimate the impact these could have on the bulk viscosity. A constant crystallinity was used for simplicity in Fig. 3, if changing crystallinity is taken into account, however, this would only accentuate the rheological fluctuations observed in Fig 3, since colder temperatures will yield higher crystal contents and vice-versa.

References for appendix

Bucholz, C. E., Gaetani, G. A., Behn, M. D. & Shimizu, N. (2013). Post-entrapment modification of volatiles and oxygen fugacity in olivine-hosted melt inclusions. Earth and Planetary Science Letters. Elsevier 374, 145–155.

Johnson, E. A. & Rossman, G. R. (2013). The diffusion behavior of hydrogen in plagioclase feldspar at 800–1000°C: Implications for re-equilibration of hydroxyl in volcanic phenocrysts. American Mineralogist 98, 1779–1787.

Johnson, E. A. (2005) Magmatic water contents recorded by hydroxyl concentrations in plagioclase phenocrysts from Mount St. Helens, 1980-1981. Geochimica et Cosmochimica Acta, 69(10s), A743.

Rader, E. L., and Larsen, J. F., 2013, Experimental phase relations of a low MgO Aleutian basaltic andesite at XH2O=0.7-1: Contributions to Mineralogy and Petrology, v. 166, no. 6, p. 1593-1611.

Papale P, Moretti R, Barbato D (2006) The compositional dependence of the saturation surface of H2O + CO2 fluids in silicate melts. Chemical Geology 229, 78-95.

Zhang, Y. X., Xu, Z. J., Zhu, M. F., and Wang, H. Y., 2007, Silicate melt properties and volcanic eruptions: Reviews of Geophysics, v. 45, no. 4.

Global Volcanism Program, 2013. Kelut (263280) in Volcanoes of the World, v. 4.5.0. Venzke, E (ed.). Smithsonian Institution. Downloaded 01 Oct 2015 (http://volcano.si.edu/volcano.cfm?vn=263280). http://dx.doi.org/10.5479/si.GVP.VOTW4-2013

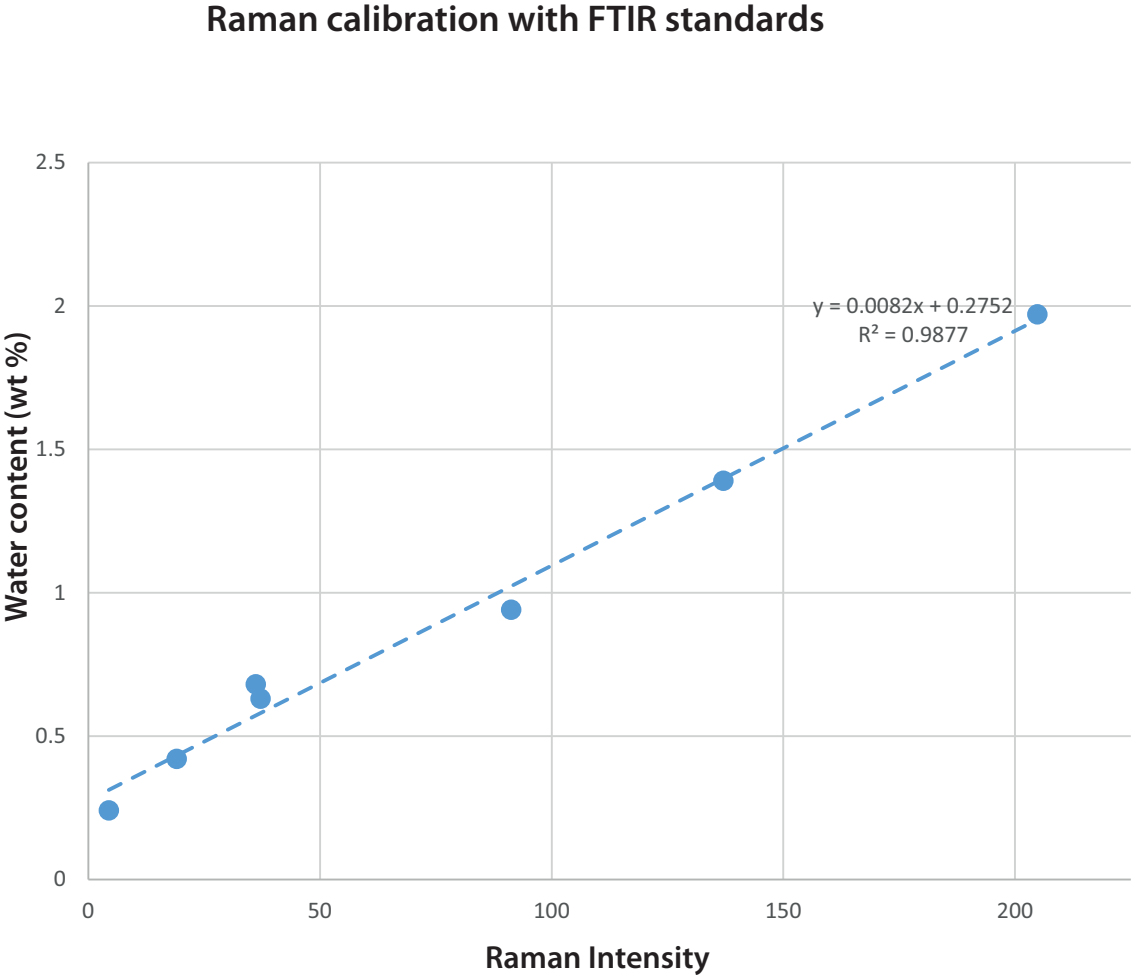

Fig. DR1. Dacitic glasses of known water contents (measured via FTIR), were measured with Raman spectroscopy (repeated ~5 times and averaged, Table DR1). Two Kelud melt inclusions were also measured both with Raman and FTIR (the two central points on the graph), providing calibration for the exact composition. The calculated intensities show a good fit (R2= 0.99) and thus were used to produce a calibration curve.

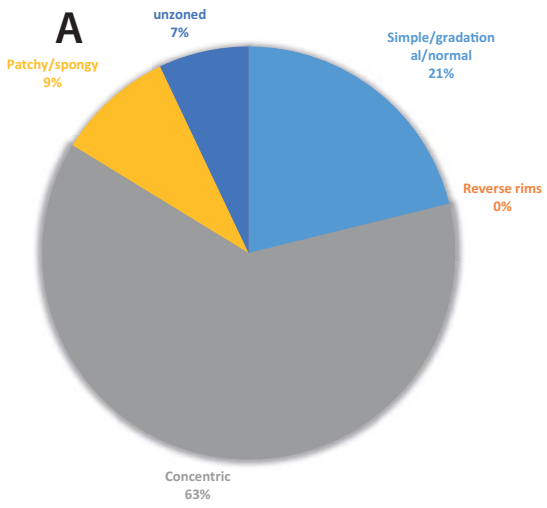

Type of zoning	Number
Simple/normal	69
Reverse rims	0
Concentric	204
Patchy/spongy	30
unzoned	23
Total	**326**

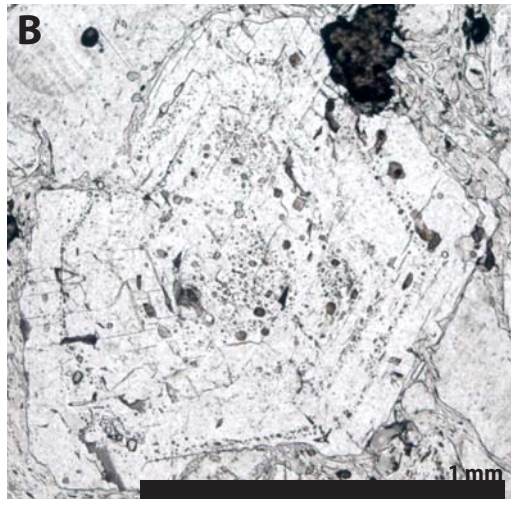

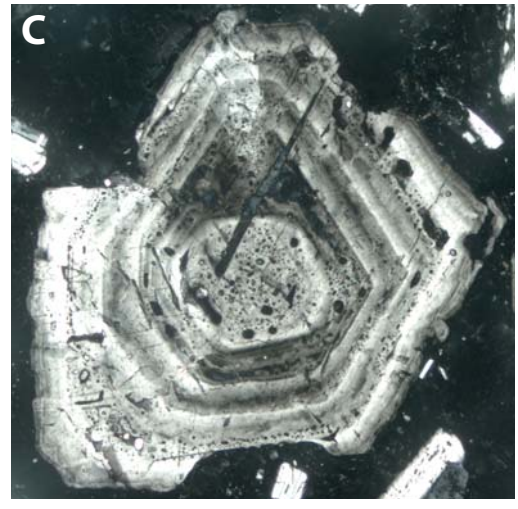

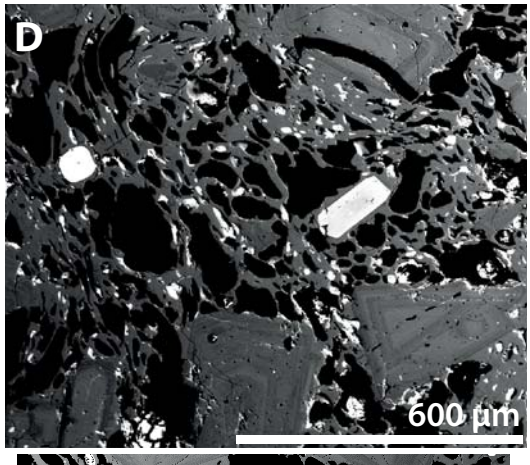

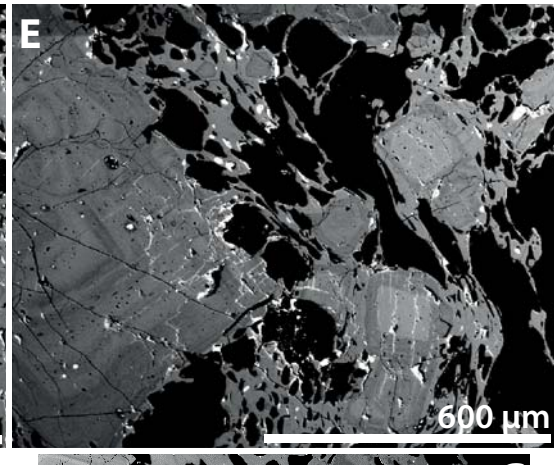

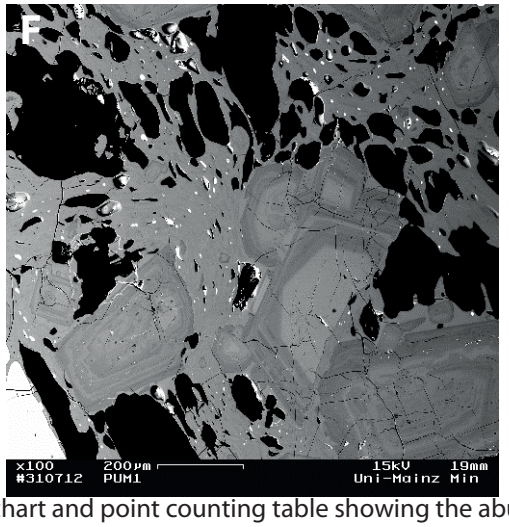

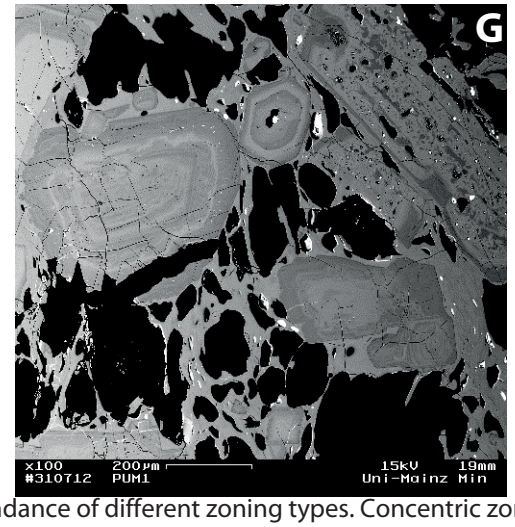

Figure DR2. A) Pie chart and point counting table showing the abundance of different zoning types. Concentric zoning is the most abundant, with normal zoning, patchy zoning, unzoned plagioclases also present. B) a plane-polarized and C) cross-polarized microscope image showing an example of a concentrically zoned plagioclase. The plagioclase shows melt inclusions entrapped within the different zoned layers. D to G) Representative backscattered SEM images showing the types of plagioclase zoning observed in the 2014 pumice. D) showing dominantly concentric zoning, E) concentric, unzoned and normal zoning, F) normal and concentric and G) concentric and patchy zoning. The groundmass glass can also be seen showing little microlite crystallisation.

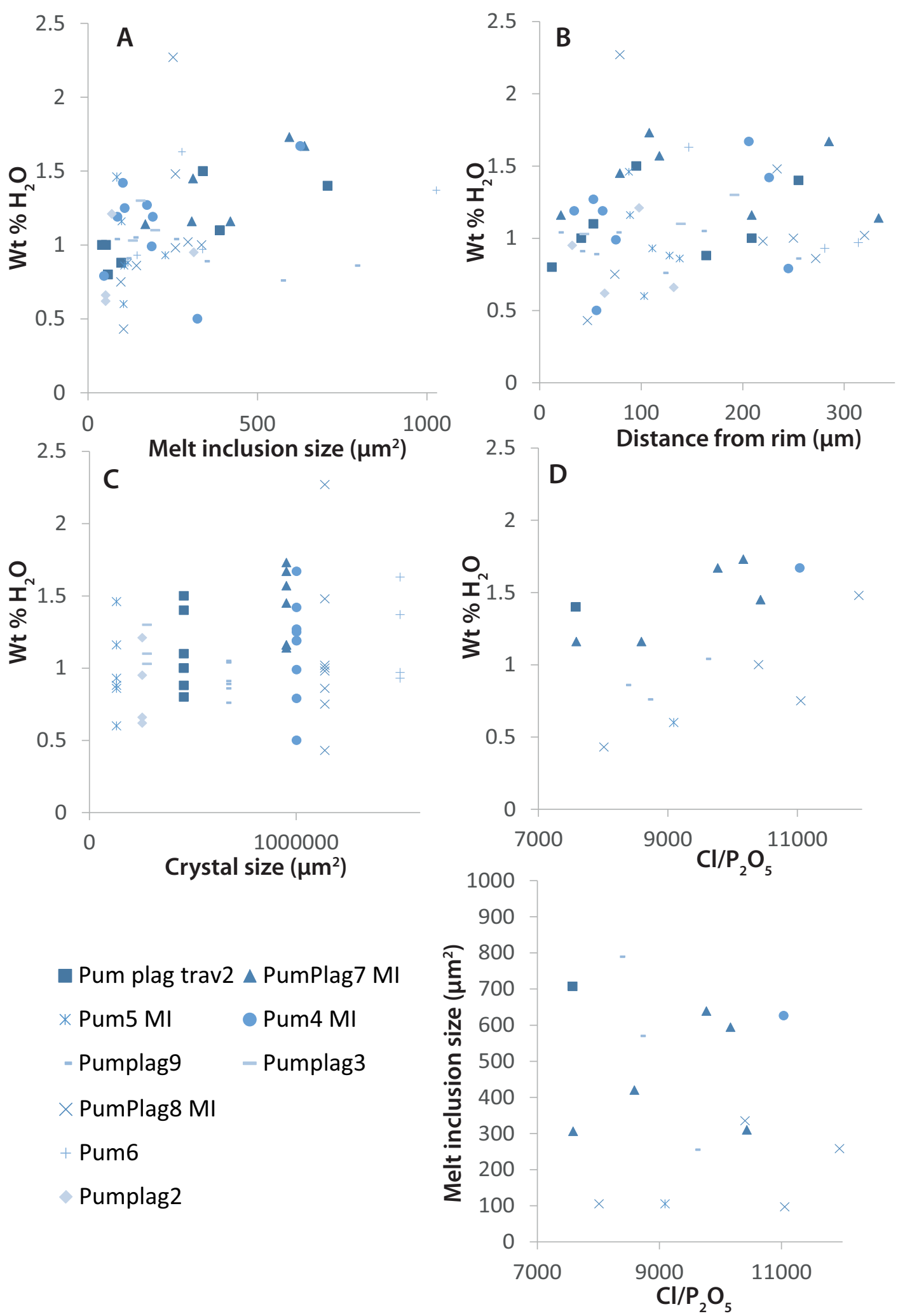

Fig. DR3. Plots of water content via Raman spectroscopy against A) melt inclusion area, B) distance from the rim, C) crystal size and D) Cl/P_2O_5, a proxy for boundary layer effects (Baker, 2008). No significant correlations between these variables are observed (n=54, all P values >0.01 for 9 different crystals). This dataset also includes crystals which did not show concentric zoning.

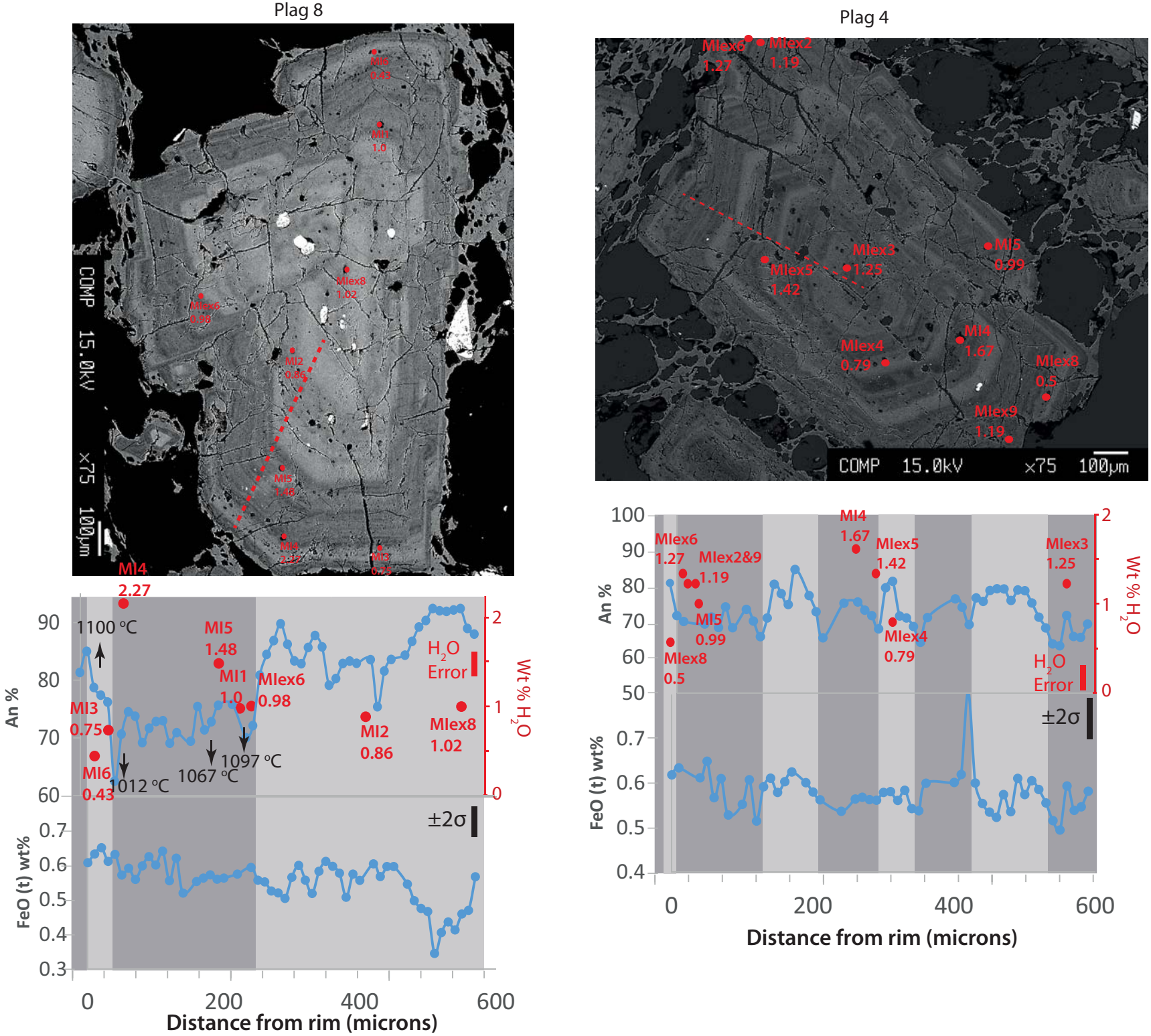

Figure DR4. Concentrically zoned plagioclase feldspars as displayed like figure 1 in the manuscript, with upper panel displaying the backscattered SEM image of the feldspar with the melt inclusions measured with Raman spectros-copy and the location of the plagioclase traverses. The lower plots show the plagioclase anor-thite and FeO chemical profile and the secondary Y axis shows the water contents throughout the crystal as measured by Raman on melt inclusions. Tem-peratures, where given are calcu-lated from Waters and Lange 2015, from plagioclase, melt inclusion compositions and water contents.

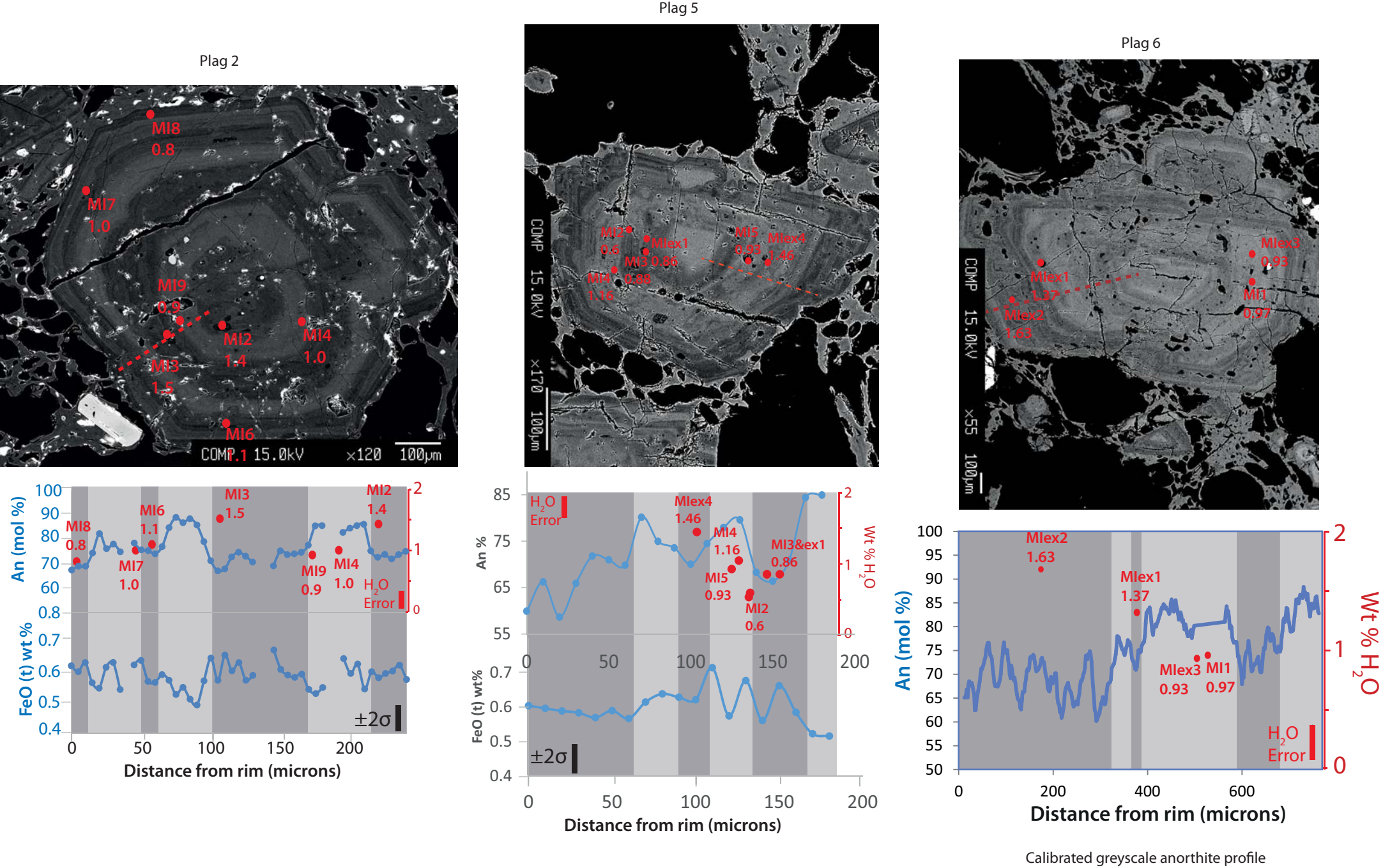

Calibrated greyscale anorthite profile

Figure DR5. Concentrically zoned plagioclase feldspars as displayed like figure 1 in manuscript, with upper panel displaying the backscattered SEM image of the feldspar with the melt inclusions measured with Raman spectroscopy and the location of the plagioclase traverse. The lower plots show the plagioclase anorthite and FeO chemical profile and the secondary Y axis shows the water contents throughout the crystal as measured by Raman on melt inclusions. Plag 6 is calculated using the strong correlation of anorthite to greyscale, which calibrated using point data of the crystal.

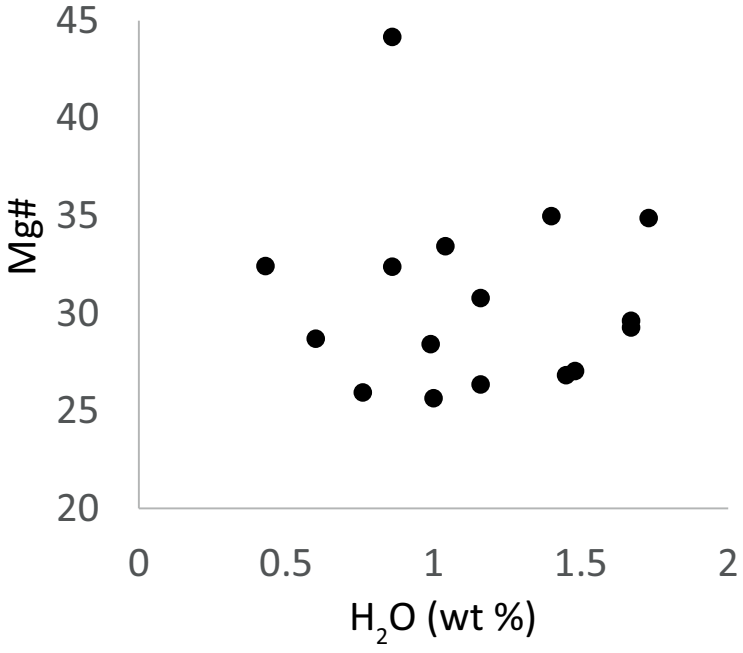

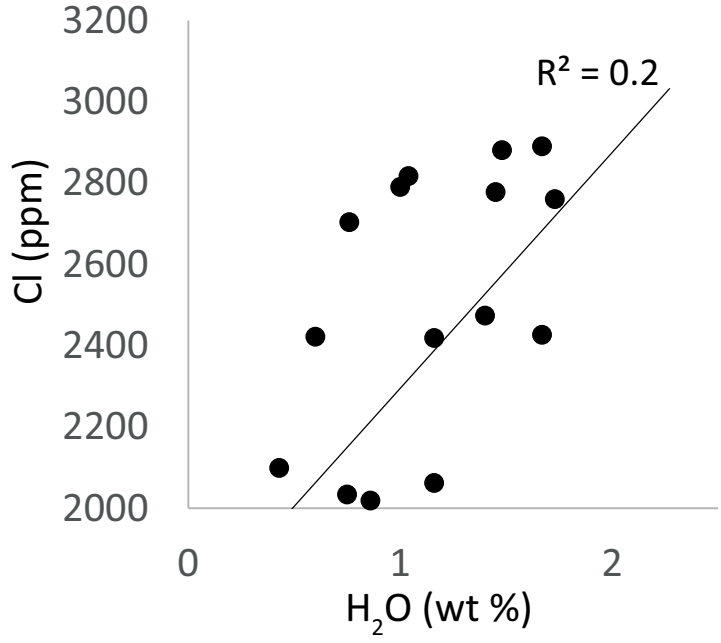

Fig DR6. a) No significant relationship exists between Mg# and H2O (p value= 0.53) implying that magma reservoirs are recharged by melts of a similar composition. b) When H2O is plotted against Cl (another incompatible element, there is a weak, but positive correlation (R2= 0.2, p value= 0.07). This supports the notion that the observed water trends measured in the melt inclusions are illustrative of volatile dilution and enrichment within the magma reservoir.

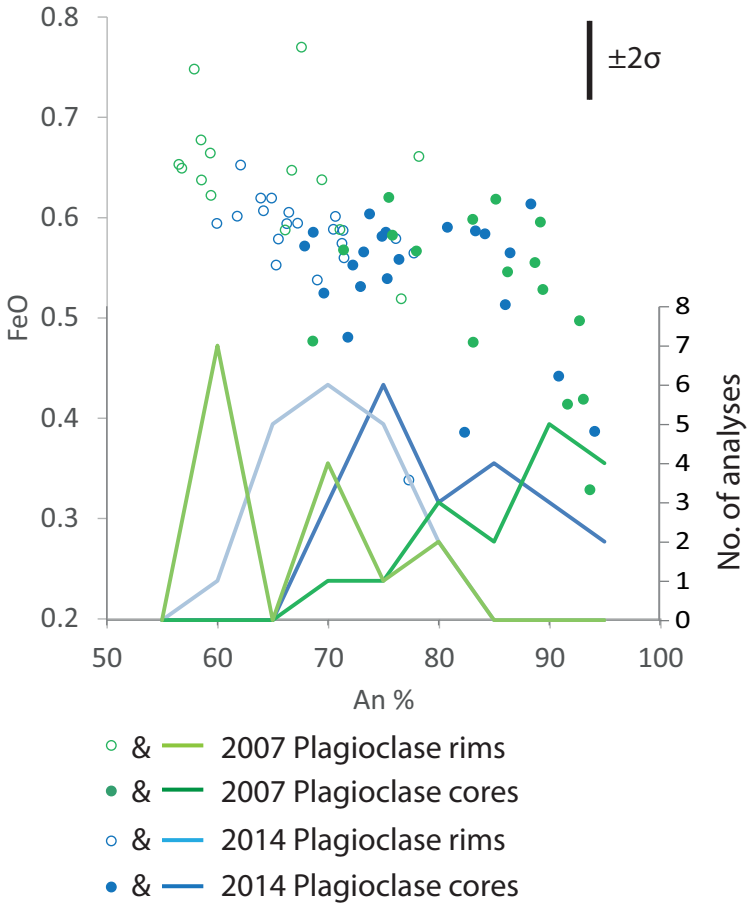

Figure DR7. Scatter plot of plagioclase phenocryst cores and rims from 2007 effusive eruption and 2014 explosive eruption. The lines show a histogram plot for molar anorthite for the same fields plotted on the right axis.

Fig 3A in Waters and Lange, 2015

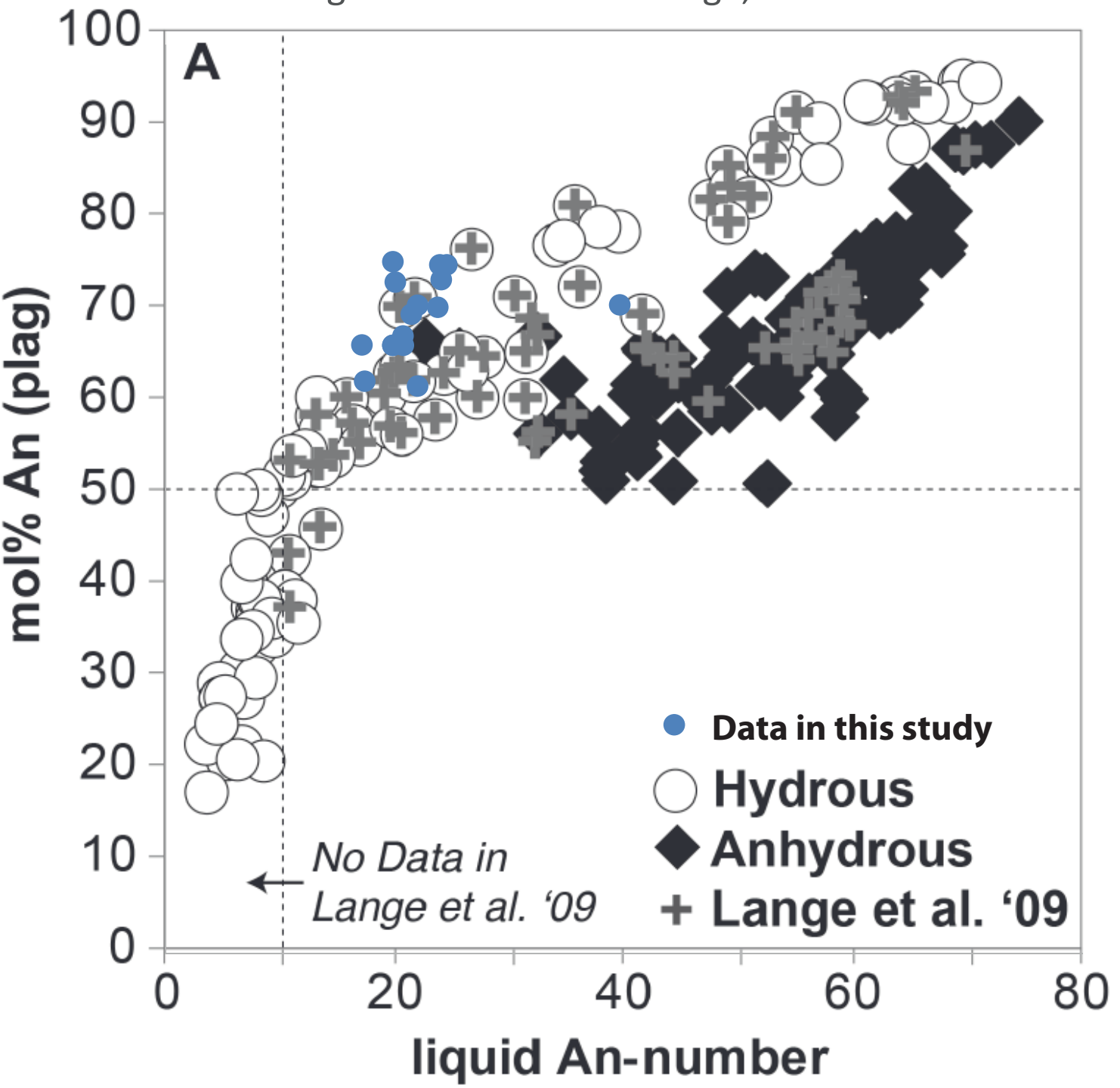

Figure DR8. Plot from Waters and Lange 2015 of liquid anorthite number versus molar anorthite to assess equilibrium of measured melt and plagioclase compositions. Those points far outside the experimental dataset in the paper were discarded as being xenocrystic or not in equilibrium with the carrier melt and thus not used for the plagioclase thermometry.

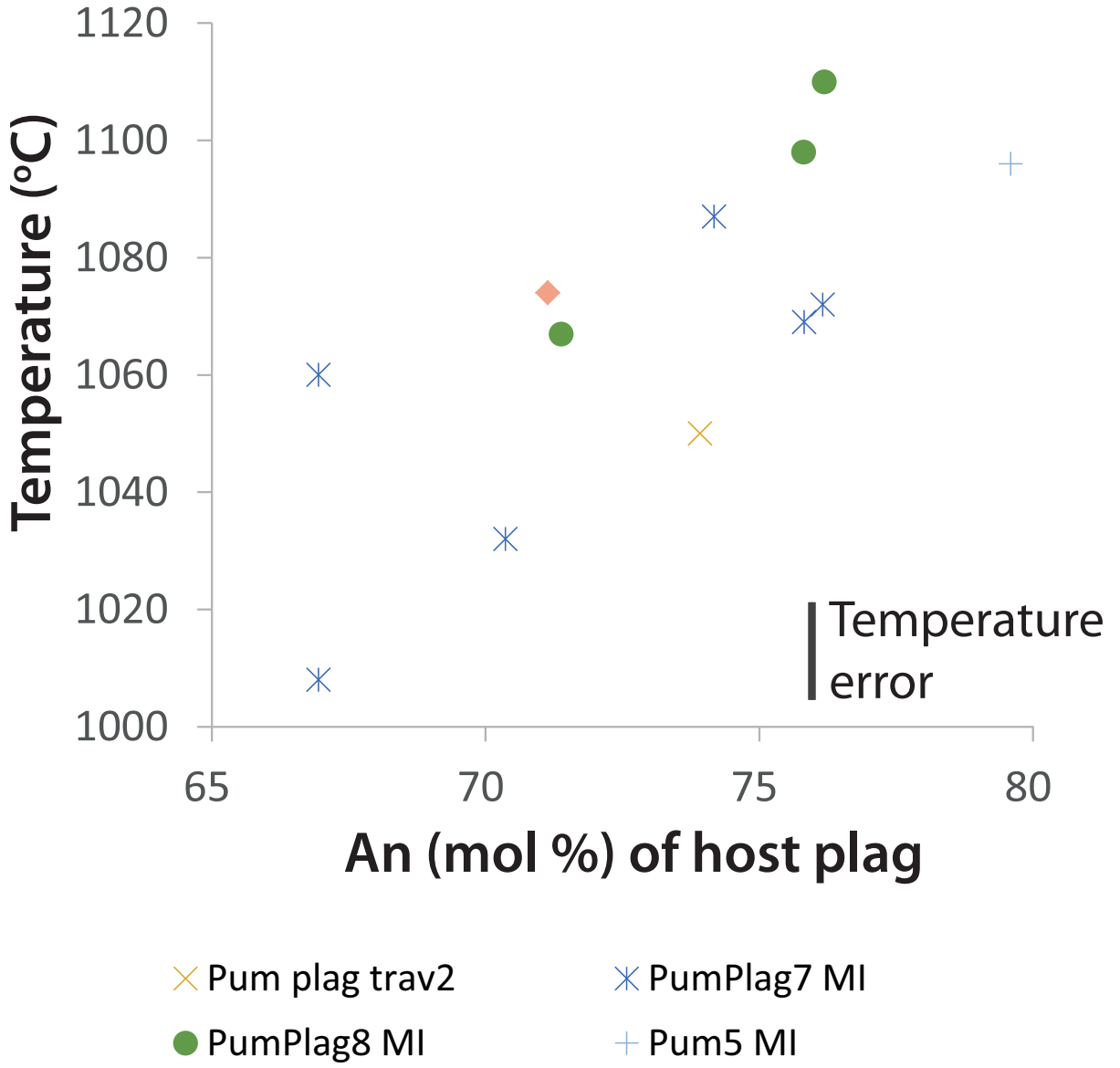

Fig. DR9. Temperature estimates from plagioclase-liquid thermometry (Waters and Lange, 2015) using plagioclase and melt inclusion compositions (where measured), and measured water contents. These temperatures are plotted against anorthite of the host plagioclase. Also plotted are the crystals from where the MI are hosted.

Table DR1. Samples with known water contents measured with Raman spectroscopy multiple times

	Repetitions of runs with Raman Spectroscopy intensities								
Samples	**1**	**2**	**3**	**4**	**5**	**Average**	**st dev**	**Stdev converte**	**Standard error of the mean**
GC101	35.12	34.74	32.51	42.47		36.21	3.75	0.31	0.15
SD401	17.83	19.47	17.58	21.74		19.15	1.66	0.29	0.14
OD201	201.02	233.90	190.44	231.57	167.44	204.87	25.22	0.48	0.22
SD301	31.30	59.64	25.05	21.71	48.49	37.24	14.51	0.39	0.18
Andglass_axial	4.19	4.73	4.49	4.47		4.47	0.19	0.28	0.14
								Average SE	**0.17**

Data for Fig. DR3 Raman calibration plot

	Average Raman in	Water conc from FTIR
GC101	36.20955	0.68
SD401	19.154125	0.42
OD201	204.8721	1.97
SD301	37.23918	0.63
Andglass_axial	4.46965	0.24
FTIRPlagMI20	137.0848	1.39
FTIRPlagMI21b	91.2876	0.94

Table DR2 Major element data from EMPA for melt inclusions and matrix glass from the 2014 eruption products

Melt Inclusions

Na2O	SiO2	CaO	FeO	P2O5	F	MgO	K2O	MnO	Cl	Al2O3	SO3	TiO2	Total
4.33	68.24	3.35	2.47	0.2232	0.0541	0.2072	1.61	0.0867	0.1797	15.94	0.0898	0.4663	97.2
4.28	68.17	2.68	2.65	0.3243	0.0801	0.4344	1.85	0.1003	0.1805	15.83	0.0434	0.5163	97.1
3.96	70.53	2.23	1.2814	0.0776	0.1776	0.2	1.99	0.0721	0.2152	15	0.0081	0.5093	96.3
3.94	70.21	2.36	1.37	0.0636	0.0736	0.2064	1.88	0.1313	0.2238	15.44	0.0192	0.4807	96.4
4.36	67.22	2.5	3.35	0.1784	0	0.5102	1.88	0.1224	0.1905	15.38	0.0421	0.6187	96.4
4.45	67.45	2.81	1.87	0.2324	0	0.3315	1.72	0.067	0.205	16.47	0.0744	0.6044	96.3
4.18	67.71	2.5	2.8	0.2115	0.035	0.3958	1.82	0.1218	0.2032	15.72	0.0512	0.5694	96.3
3.95	67.58	2.7	3.35	0.1042	0.1369	0.5533	1.71	0.154	0.181	15.07	0.0665	0.3885	95.9
2.04	69.53	2.81	2.43	0.2	0	0.5649	1.6	0.1242	0.1784	15.62	0.0293	0.5435	95.7
3.38	66.26	2.53	4.51	0.1149	0	1.2962	2.55	0.1952	0.3	13.52	0.0291	0.3939	95.1
3.49	65.98	2.86	4.39	0.1534	0	1.1229	2.36	0.2554	0.2816	13.72	0.0253	0.4689	95.1
3.54	65.81	2.73	4.03	0.237	0.0178	1.1058	2.21	0.1775	0.2863	14.29	0.0753	0.5897	95.1
3.34	69	2.87	4.33	0.2642	0	0.9015	1.87	0.1777	0.2177	12.42	0.0158	0.652	96.1
2.21	68.72	3.33	4.46	0.2464	0	1.2035	1.69	0.2322	0.2142	13.62	0.0481	0.6055	96.6
4.34	66.13	3.31	3.79	0.2199	0.1165	0.8942	1.82	0.1588	0.2427	14.78	0.0383	0.5026	96.4
5.36	61.2	6.32	3.07	0.162	<0.098	0.6836	1.0637	0.0668	0.1016	19.02	0.0461	0.427	97.5
4.16	66.63	2.68	4.97	0.2716	<0.108	1.4927	2.33	0.2019	0.2761	13.83	0.0398	0.5931	97.5
4.27	66.8	2.86	3.71	0.2663	<0.103	0.763	2.04	0.1416	0.2778	14.04	0.0358	0.6038	95.8
3.66	65.88	2.78	4.43	0.2959	<0.108	1.0279	2.07	0.1931	0.2891	13.48	<0.036	0.6845	94.8
4.73	67.25	3.68	4.64	0.2718	0.1352	1.1571	1.47	0.1111	0.2062	13.94	0.0492	0.5978	98.2
3.97	66.11	2.97	3.34	0.2411	<0.112	0.6944	1.96	0.16	0.2881	13.75	0.0396	0.6895	94.2
4.49	66.87	2.16	4.3	0.184	<0.106	0.0531	2.6	<0.052	0.2034	14.47	<0.033	0.4987	95.9
4.63	58.8	6.86	4.21	0.2168	0.1377	1.1311	1.65	0.1404	0.1587	19.69	0.0385	0.511	98.2
3.86	66.09	3.38	4.28	0.2683	<0.097	0.8282	1.9	0.1886	0.2791	13.74	0.0496	0.6765	95.6
3.79	68.91	2.58	3.2	0.2664	<0.097	0.7225	2.08	0.1233	0.2422	12.75	0.0517	0.6628	95.4
3.19	64.32	2.02	6.29	0.2415	0.1737	2.79	2.79	0.1335	0.2019	12.16	0.0514	0.5926	95.0
3.95	66.64	2.81	3.75	0.3109	<0.104	0.7367	2.06	0.2008	0.2704	13.34	0.0358	0.6826	94.8
4.25	65.75	2.69	4.22	0.3265	<0.101	1.2735	2.25	0.164	0.2474	14.05	0.0412	0.6418	95.9
5.02	68.66	3.95	3.39	0.1877	<0.108	0.6182	1.39	0.1149	0.1476	15.53	<0.035	0.4928	99.5
4.18	65.74	2.89	4.38	0.1469	<0.104	1.2724	2.01	0.1587	0.2438	14.06	0.0673	0.5369	95.7
3.04	67.85	3.13	4.35	0.2816	<0.106	0.8726	1.5	0.2077	0.2419	12.43	<0.037	0.6745	94.6

4.3	64.72	3.02	4.38	0.262	<0.101	1.1783	2.02	0.1949	0.2099	14.62	0.0399	0.5311	95.5
MATRIX GLASS													
4.42	69.73	3.61	3.91	0.2266	0.0742	1.0624	1.68	0.1806	0.1452	15.39	0.0068	0.5891	101.0
4.14	69.59	3.56	3.85	0.195	0	1.0094	1.83	0.2022	0.1313	15.48	0	0.513	100.5
4.3	69.52	3.61	4.22	0.1993	0	1.1318	1.75	0.1282	0.1283	15.71	0.0052	0.5685	101.3
4.29	69.35	3.68	4.29	0.1992	0.0121	1.1154	1.75	0.1446	0.1135	15.6	0.0077	0.5469	101.1
4.35	69.71	3.54	4.02	0.1758	0.0002	1.0875	1.68	0.1314	0.1159	15.68	0	0.5183	101.0
4.34	69.58	3.78	3.89	0.2186	0.0213	1.0466	1.63	0.1198	0.1297	15.76	0.0447	0.4715	101.0
4.42	69.35	3.5	4.04	0.2121	0.0322	1.0498	1.79	0.1797	0.13	15.55	0.0362	0.5324	100.8
4.21	69.23	3.37	3.87	0.1914	0.008	0.985	1.74	0.1248	0.1085	15.31	0.0388	0.5471	99.7
4.24	65.97	3.38	3.88	0.211	0	1.0007	1.62	0.157	0.1455	14.55	0	0.4999	95.7
4.38	70.03	3.61	4.03	0.204	0	1.0835	1.76	0.1858	0.1158	15.6	0.0071	0.4944	101.5
4.28	69.43	3.63	4.14	0.1954	0	1.0611	1.66	0.1983	0.1277	15.41	0.0254	0.5299	100.7
4.28	69.32	3.5	4.1	0.1702	0.0332	1.1212	1.67	0.1281	0.1324	15.49	0.0151	0.5843	100.5
4.41	69.7	3.66	4.02	0.197	0	1.063	1.73	0.1541	0.1252	15.73	0.0112	0.5189	101.3
4.24	69.37	3.57	4.03	0.1922	0.1757	1.0485	1.71	0.1791	0.1289	15.48	0	0.5134	100.6
4.45	69.54	3.51	3.92	0.2507	0.0135	0.9919	1.82	0.1579	0.0849	15.67	0	0.5566	101.0
4.24	69.55	3.46	3.82	0.1931	0.1654	1.0472	1.82	0.1024	0.1112	15.39	0.0446	0.5521	100.5
4.23	69.54	3.42	3.94	0.1534	0	1.0158	1.83	0.1749	0.1307	15.41	0.0039	0.5529	100.4
4.19	69.73	3.5	4.34	0.189	0	1.1104	1.68	0.1088	0.1737	14.58	0.0157	0.5937	100.2
3.52	70.01	3.42	3.72			0.7115	1.84	0.1577		15.22		0.45	99.0

Table DR3. Diffusion timescales using the modified model from Bucholz et al 2013 using differing conditions. These conditions used were specifically recorded in this study (Table S4) and therefore not arbitrary. This was done so that we could explore the full range of timescales estimated for the exact conditions appropriate for this study. Two different published KD's (diffusivities) for hydrogen in plagioclase were also used.

Inclusion size (dian	Crystal size	Temperature	H2O intital	H2O end	KD Hamada ((	KD Johnson (0.004)
17.5	489	1000	1.14	1.45	9 days	20 days
17.5	613	1000	1.14	1.45	10 days	20 days
17.5	181	1000	1.14	1.45	7 days	18 days
46	421	1000	1.14	1.45	49 days	120 days
46	613	1000	1.14	1.45	51 days	123 days
46	181	1000	1.14	1.45	44 days	110 days
46	421	1090	1.14	1.45	9 days	21 days
46	421	985	1.14	1.45	67 days	164 days
46	421	1000	1.14	1.91	55 days	136 days
17.5	421	1000	1.14	1.91	9 days	21 days
46	613	1000	1.14	1.91	57 days	140 days

Table DR4. Raman data of water contents with information regarding the melt inclusion and crystal size and EMPA data

									EMPA data													
Concentric-zoned crystals		**H2O (Raman)**	**An of host pla**	**Fe of host pla**	**Crystal size (u**	**Modelled ten**	**Distance from**	**Size of MI**	**Na2O**	**SiO2**	**K2O**	**FeO**	**P2O5**	**FxOy**	**MgO**	**CaO**	**MnO**	**ClxOy**	**Al2O3**	**SO3**	**TiO2**	**Mg# number**
Pum plag trav2	Pumplag2 MI2	1.4	73.9	0.62	456406	1050.00	255	707	4.25	65.75	2.25	4.22	0.327	0.101	1.274	2.69	0.164	0.247	14.05	0.041	0.642	34.98
	MI4	1	85.8	0.63	456406		209	41														
	MI3/5	1.5	67.2	0.57	456406		95	339														
	MI6	1.1	74.3	0.57	456406		53	389														
	MI7	1	75.9	0.64	456406		41	53														
	MI8	0.8	69.2	0.60	456406		12	59														
	MI9	0.88	85.8	0.53	456406		164	98														
PumPlag7 MI	Pumplag7 MI1	1.14	76.2	0.58	952896	1072.00	334	169														
	MI7	1.67	70.4	0.59	952896	1032.00	285	639	3.66	65.88	2.07	4.43	0.296	0.108	1.028	2.78	0.193	0.289	13.48	0.036	0.685	29.26
	MI9	1.16	74.2	0.58	952896	1087.00	209	306	4.73	67.25	1.47	4.64	0.272	0.135	1.157	3.68	0.111	0.206	13.94	0.049	0.598	30.78
	MI6	1.45	67.0	0.61	952896	1060.00	79	310	4.27	66.8	2.04	3.71	0.266	0.103	0.763	2.86	0.142	0.278	14.04	0.036	0.604	26.83
	MI5	1.73	67.0	0.61	952896	1008.00	108	594	4.16	66.63	2.33	4.97	0.272	0.108	1.493	2.68	0.202	0.276	13.83	0.040	0.593	34.87
	MI4	1.16	75.8	0.58	952896	1069.00	21	420	3.04	67.85	1.5	4.35	0.282	0.106	0.873	3.13	0.208	0.242	12.43	0.037	0.675	26.34
	MI8	1.57	67.0		952896		118	2109														
PumPlag8 MI	Pumplag8 MI2	0.86	82.9	0.56	1139286	bd	272	143	4.63	58.8	1.65	4.21	0.217	0.138	1.131	6.86	0.140	0.159	19.69	0.039	0.511	32.39
	MI5	1.48	71.4	0.57	1139286	1067.00	234	258	3.97	66.11	1.96	3.34	0.241	0.112	0.694	2.97	0.160	0.288	13.75	0.040	0.690	27.04
	MI1	1	75.8	0.57	1139286	1098.00	250	335	3.86	66.09	1.9	4.28	0.268	0.097	0.828	3.38	0.189	0.279	13.74	0.050	0.677	25.65
	MI4	2.27	62.5	0.57	1139286		79	251														
	MI3	0.75	76.2	0.63	1139286	1110.00	74	97	4.49	66.87	2.6	4.3	0.184	0.106	0.053	2.16	<0.052	0.203	14.47	0.033	0.499	2.15
	MI6	0.43	85.0	0.63	1139286	bd	47	105	4.3	64.72	2.02	4.38	0.262	0.101	1.178	3.02	0.195	0.210	14.62	0.040	0.531	32.41
	MIex6	0.98	89.0	0.47	1139286		220	258														
	MIex8	1.02	72.1	0.56	1139286		320	295														
Pum5 MI	Pumplag5 MI3	0.88	68.3	0.56	130519		128	118														
	MI2	0.6	79.6	0.68	130519	1096.00	103	105	3.79	68.91	2.08	3.2	0.266	0.097	0.723	2.58	0.123	0.242	12.75	0.052	0.663	28.70
	MI4	1.16	77.9	0.57	130519		89	99														
	MI5	0.93	77.9	0.57	130519		111	228														
	MIex1	0.86	79.6	0.68	130519		138	107														
	MIex4	1.46	75.0	0.64	130519		88	85														
Pum4 MI	Pumplag4 MI4	1.67	71.1	0.58	1002022	1074.00	206	626	4.34	66.13	1.82	3.79	0.220	0.117	0.894	3.31	0.159	0.243	14.78	0.038	0.503	29.61
	MI5	0.99	71.4	0.65	1002022	bd	75	188	5.36	61.2	1.0637	3.07	0.162	0.098	0.684	6.32	0.067	0.102	19.02	0.046	0.427	28.42
	MIex3	1.25	71.8	0.59	1002022		360	108														
	MIex4	0.79	81.4	0.58	1002022		245	47														
	MIex5	1.42	68.1	0.56	1002022		226	103														
	MIex2	1.19	69.4	0.61	1002022		62	191														
	MIex9	1.19	69.4	0.61	1002022		34	87														
	MIex6	1.27	70.1	0.63	1002022		53	174														
	MIex8	0.5	81.0		1002022		56	323														
Pum6	Pumplag6 MI1	0.97	83.0		1503561		314	338														
	MIex3	0.93	83.0		1503561		281	145														
	MIex1	1.37	71.0		1503561		361	1028														
	MIex2	1.63	65.0		1503561		147	277														
Non-concentric zoned crystals																						
Pumplag9	Pumplag9 MI1	0.86	67		663816	985.00	253	789	3.19	64.32	2.79	6.29	0.242	0.174	2.790	2.02	0.134	0.202	12.16	0.051	0.593	44.16
	MI2	0.76	68		663816	1091.00	122	570	3.95	66.64	2.06	3.75	0.311	0.104	0.737	2.81	0.201	0.270	13.34	0.036	0.683	25.94
	MI3	1.04	81		663816		19	80														
	MI4	1.05	71		663816		160	135														
	MI5	0.91	77		663816		40	114														
	MI6	0.89	77		663816		54	345														
	MI7	1.04	63		663816	1025.00	76	255	3.67	64.45	2.27	4.92	0.294	0.153	1.386	2.19	0.146	0.282	12.4	0.046	0.697	33.43
Pumplag3	MI6	1.1			278237		139	198														
	MI5	1.3			278237		192	155														
	MI3	1.03			278237		44	132														
Pumplag2	MI3	0.66			255285		132	52														
	MI4	1.21			255285		98	70														
	MI5	0.95			255285		32	312														
	MI7	0.62			255285		64	52														

Table DR5. FTIR data from melt inclusions. Not all CO2 vaules could be measured, as some were below detection limit or unresolvable due to poor spectral resolution

	H2O wt %	CO2 (ppm)
2014PumMI1	1.27	336
2014PumMI1 0004	1.31	279
2014PumMI1 0005	0.525	33
2014PumMI1 0007	1.075	325
2014PumMI1 0010	0.455	
2014PumMI1 0012	1.725	
2014PumMI1 0014	1.6	
2014PumMI1 0020	1.33	
2014PumMI1 0021	0.9	
2014PumMI1 0013	0.43	57
2014PumMI1 0018	2.33	
2014PumMI1 0019	0.88	323
2014PumMI1 0022	0.76	
Min	0.43	
max	2.33	
average	1.12230769	